To cite this article: HE P P, LI Z R, ZHANG X W, et al. Influence of subgrid-scale models on cavitation phenomenon around a 3D twisted hydrofoil[J/OL]. Chinese Journal of Ship Research, 2022, 17(3). http://www.ship-research.com/en/article/doi/10.19693/j.issn.1673-3185.02387.

DOI: 10.19693/j.issn.1673-3185. 02387

Influence of subgrid-scale models on cavitation phenomenon around a 3D twisted hydrofoil

HE Pengpeng[1,2], *LI Ziru*[1,2], *ZHANG Xiaowang*[1,2], *HE Wei*[*1,2]

1 Key Laboratory of High Performance Ship Technology of Ministry of Education, Wuhan University of Technology, Wuhan 430063, China

2 School of Naval Architecture, Ocean and Energy Power Engineering, Wuhan University of Technology, Wuhan 430063, China

Abstract: [**Objective**] This paper aims to explore the suitability of grid density and subgrid-scale (SGS) models in the numerical simulation of cavitation of a three-dimensional (3D) twisted hydrofoil. [**Methods]** The large eddy simulation (LES) method and Schnerr-Sauer (S-S) cavitation model are used to simulate the unsteady cavitating flow field of a Delft Twist11N 3D twisted hydrofoil. Three sets of grids with different densities and three SGS models, namely, algebraic wall-modeled LES (WMLES) model, Smagorinsky-Lilly (SL) model, and wall-adapting local eddy-viscosity (WALE) model are mainly studied to identify their influence on the cavitation evolution process, cavitation shedding frequency, and time averaged lift and drag coefficients of the hydrofoil. [**Results**] The results show that appropriate grid refinement can not only capture more unsteady cavitation evolution phenomena such as the shedding of small-scale cavities and the inception and collapse of horseshoe-shaped cloud cavities but also obtain more precise cavitation shedding frequency, time averaged lift and drag coefficients, and time averaged pressure distribution. Compared with WMLES and SL models, the WALE model better captures the evolution of sheet and cloud cavities and has better accuracy in predicting the cavitation shedding frequency, time averaged lift and drag coefficients, and time averaged pressure coefficient. [**Conclusion**] It is recommended to adopt the LES method based on the WALE model for the numerical simulation of unsteady cloud cavitation.

Key words: three-dimensional twisted hydrofoil; cloud cavity; large-eddy simulation; subgrid-scale model; grid density

CIC number: U664.33

0 Introduction

In terms of ships, propeller cavitation not only deteriorates propulsion performance but also leads to severe noise, vibration, and cavitation erosion. In addition, the cavitation pattern of the propeller varies at different radii due to its three-dimensional (3D) twisted shape. In order to accurately predict the propeller's cavitation erosion and cavitation noise, it is necessary to discuss the inception and collapse mechanisms of unsteady cloud cavitation. Numerous researchers have carried out numerical

Received: 2021 − 05 − 24 **Accepted**: 2022 − 03 − 13

Supported by: Fundamental Research Funds for the Central Universities of China (215202001, 2019III076GX); Major International (Regional) Joint Research Project of NSFC (51720105011); Key Program of National Priority Research Area Foundation (61402070105)

Authors: HE Pengpeng, male, born in 1991, Ph.D. candidate. Research interest: hydrodynamic performance of ship propulsion. E-mail: hepengpengemail@163.com

LI Ziru, female, born in 1983, Ph.D., associate professor. Research interest: hydrodynamic performance of ship propulsion. E-mail: lisay333@163.com

ZHANG Xiaowang, male, born in 1994, master degree candidate. Research interest: hydrodynamic performance of ship propulsion. E-mail: 836221248@qq.com

HE Wei, male, born in 1982, Ph.D., associate professor. Research interest: hydrodynamic performance of ship propulsion. E-mail: hwcudca@163.com

***Corresponding author**: HE Wei

simulations and experiments on 3D twisted hydrofoils with varied angles of attack in the spanwise direction to better observe and understand the evolution process of unsteady cloud cavitation.

For instance, by using laser doppler velocimetry (LDV), high-speed photography, and particle image velocimetry (PIV) technologies, researchers in Refs. [1-3] investigated the cavity shapes, angles of attack, cavitation number, and cavity inception and shedding of 3D hydrofoils in cavitation water tunnels. In the experiments, horseshoe-shaped cavities were observed, and it was found that the angles of attack and the cavitation number have the most to do with the flow characteristics of cavitation. The side-entrant jet was introduced in the investigation of a Delft Twist11N 3D twisted hydrofoil in Ref. [4], and the experimental results were used to analyze the role of the side-entrant jet and the re-entrant jet in cavity shedding. In Refs. [5-8], the cavitation phenomenon around the Twist11N hydrofoils was numerically simulated by utilizing turbulence models such as SST k-ω and RNG k-ε modified by turbulent viscosity and cavitation models including Schnerr-Sauer (S-S), Singhal, and Zwart, and large-scale cavity shedding was simulated by using the Reynolds-Averaged Navier-Stokes (RANS) method modified by viscosity. However, there was a considerable discrepancy between the cavitation shedding frequency and the experimental results, and the cloud cavity shape was much smaller than the experimental observations. The fundamental reason was that the RANS method performed Reynolds averaging on the characteristic parameters of turbulence at all scales and less described fine cavity structures and unsteady transient characteristics. For the inception of tip vortex cavities around the 3D hydrofoils, the SST k-ω, detached-eddy simulation (DES), and large-eddy simulation (LES) models were used to calculate the tip vortex flow field around such hydrofoils in Ref. [9]. The results demonstrated that the calculated results based on the LES method are in good agreement with the experimental values. The unsteady cavitation turbulence around a NACA 66 hydrofoil was analyzed numerically by using the LES method with high accuracy in Ref. [10]. The result confirmed that pressure pulsation is associated with cavity shedding and that cavity volume acceleration is the primary source of the pressure pulsation around the hydrofoil with cavities. In Ref. [11], the influence of grid resolution on the numerical simulation of cloud cavitating flow around a 3D twisted hydrofoil was studied by using two sets of grids with different densities. The experiment demonstrated that in terms of the cavitating flow simulation, the accuracy of fine grids is remarkably higher than that of coarse grids. On the basis of the Lagrangian viewpoint, the cavitating flow of a 3D twisted hydrofoil was analyzed in Ref. [12], and the results showed clear trajectory lines of the re-entrant jet and side-entrant jet. In Ref. [13], the ventilated cavitating flow around a NACA 66 hydrofoil was numerically studied, and the effectiveness of the numerical method was verified by comparison with experimental results. In conclusion, the division of grids and selection of SGS models still rely on the researchers' priori knowledge and lack objective evidence, though numerous numerical simulations of the cavitation around 3D twisted hydrofoils based on the LES method have been performed.

Therefore, this paper explores the suitability of grid density and SGS models in numerical simulations of cavitation phenomena around 3D twisted hydrofoils by investigating the cavitation around a Delft Twist11N twisted hydrofoil through the multiphase viscous flow numerical method based on the LES method. The paper focuses on the predictability and suitability of different grid densities and SGS models for the characteristics of such cavitating flows and analyzes the unsteady transient characteristics of the cloud cavitation around the hydrofoil. The results are expected to serve as a reference for the division of grids and selection of SGS models when the LES method is used to predict cavitation around 3D hydrofoils and propellers and facilitate the analysis of the unsteady cavitating flow field in ship propellers.

1 Mathematical models

1.1 Governing equations

In this paper, the cavitating flow including vapor and liquid phases is regarded as a single liquid with variable density, and the two phases are described by the homogeneous mixture model based on the homogeneous equilibrium flow theory. The continuity and momentum equations for the cavitating flow field with mixed vapor and liquid are as follows.

$$\frac{\partial}{\partial t}(\rho_{\mathrm{m}}) + \frac{\partial}{\partial x_j}(\rho_{\mathrm{m}}\boldsymbol{u}_j) = 0 \tag{1}$$

$$\frac{\partial(\rho_{\mathrm{m}}\boldsymbol{u}_i)}{\partial t} + \frac{\partial(\rho_{\mathrm{m}}\boldsymbol{u}_i\boldsymbol{u}_j)}{\partial x_i} = -\frac{\partial p}{\partial x_i} + \frac{\partial}{\partial x_j}\left(\mu_{\mathrm{m}}\frac{\partial \boldsymbol{u}_i}{\partial x_j}\right) \tag{2}$$

where $\boldsymbol{u}_i$ and $\boldsymbol{u}_j$ are the velocity tensors in the i and j

direction of the axis, respectively; p is the pressure; ρ_m and μ_m are the density and dynamic viscosity of the mixed flow, respectively, and their relationship with the volume fraction of vapor phase α is defined as

$$\rho_m = \alpha\rho_v + (1-\alpha)\rho_l \quad (3)$$

$$\mu_m = \alpha\mu_v + (1-\alpha)\mu_l \quad (4)$$

where subscripts m, v, and l represent mixed vapor and liquid phases, vapor phase, and liquid phase, respectively.

1.2 LES method

As cavitating flow belongs to complex turbulent flow, this paper employs the LES method with high accuracy to study it. The LES method utilizes a filter to filter the Navier-Stokes (N-S) equation and directly solves the filtered equation to obtain physical quantities of solvable scales. The physical quantities of filtered SGS are solved by corresponding SGS models. For incompressible flow, the continuity and momentum equations processed by filtering are derived as follows.

$$\frac{\partial\rho_m}{\partial t} + \frac{\partial}{\partial x_i}(\rho_m\bar{u}_i) = 0 \quad (5)$$

$$\frac{\partial}{\partial t}(\rho_m\bar{u}_i) + \frac{\partial}{\partial x_j}(\rho_m\overline{u_iu_j}) = -\frac{\partial\bar{p}}{\partial x_i} + \frac{\partial}{\partial x_j}\left(\mu_m\frac{\partial\bar{u}_i}{\partial x_j}\right) - \frac{\partial\tau_{ij}}{\partial x_j} \quad (6)$$

where components with over bars are filtered large-scale physical quantities; τ_{ij} is SGS stress and $\tau_{ij} = \rho(\overline{u_iu_j} - \overline{u_i}\,\overline{u_j})$. Based on the Boussinesq hypothesis, SGS stress is expressed as

$$\tau_{ij} = \frac{1}{3}\tau_{kk}\delta_{ij} - 2\mu_t\bar{S}_{ij} \quad (7)$$

where μ_t is the turbulent viscosity of SGS stress; τ_{kk} is the isotropic part of the SGS stress; δ_{ij} is the Kronecker delta function; $\bar{S}_{ij}$ is the rate-of-strain tensor for the solvable scale. The influence of the turbulent viscosity on SGS stress is simulated by using SGS models such as Smagorinsky-Lilly (SL) [14], wall-adapting local eddy-viscosity (WALE) [15], and algebraic wall-modeled LES (WMLES) models [16], which can be found in corresponding studies.

1.3 Cavitation model

The S-S model, which is based on the mass transport equation, is used to describe the conversion between the two phases. The cavitation model is developed based on a simplified Rayleigh-Plesset dynamics equation.

The transport equation of α is

$$\frac{\partial}{\partial t}(\rho_v\alpha) + \frac{\partial}{\partial x_j}(\rho_v\alpha u_{v,j}) = S_e - S_c \quad (8)$$

where u_v represents the flow velocity of the vapor phase; S_e and S_c are the sources terms of mass transport during the evaporation and condensation, respectively, and they are related to the growth and collapse of cavities.

When vapor pressure $p_v \geqslant p$, growth (evaporation) occurs.

$$S_e = \frac{\rho_v\rho_l}{\rho_m}\frac{3\alpha(1-\alpha)}{R_B}\sqrt{\frac{2}{3}\frac{p_v - p}{\rho_l}} \quad (9)$$

When $p_v \leqslant p$, collapse (condensation) occurs.

$$S_c = \frac{\rho_v\rho_l}{\rho_m}\frac{3\alpha(1-\alpha)}{R_B}\sqrt{\frac{2}{3}\frac{p - p_v}{\rho_l}} \quad (10)$$

where R_B is the cavity radius, and its relationship with α can be expressed as follows.

$$\alpha = n_b\frac{4}{3}\pi R_B^{\,3}\Big/\left(1 + n_b\frac{4}{3}\pi R_B^{\,3}\right) \quad (11)$$

where n_b is the cavitation number density and equals 10^{13}.

2 Models and settings

A Delft Twist11 twisted hydrofoil is taken as the research subject in this paper. As described in Ref. [4], its sections at different positions in the spanwise direction are featured with a NACA 0009 shape. After the angle of attack is designed, the angle of attack ranges from −2° at the end section to 9° at the midsection. Several views of the hydrofoil are shown in Fig. 1. Specifically, the origin of the coordinate system is located at the midpoint of the chord length of the end section of the hydrofoil, with *XC*, *YC*, and *ZC* indicating inflow direction, spanwise direction, and vertical direction, respectively. LE and TE represent the leading edge and trailing edge of the hydrofoil, respectively. The chord length C equals 0.15 m, and the span length l equals 0.30 m.

The calculated domain is shown in Fig. 2. Since the geometrical model of the Twist11 twisted hydrofoil is symmetric, only half the model is considered. The distance between the midpoint of the chord

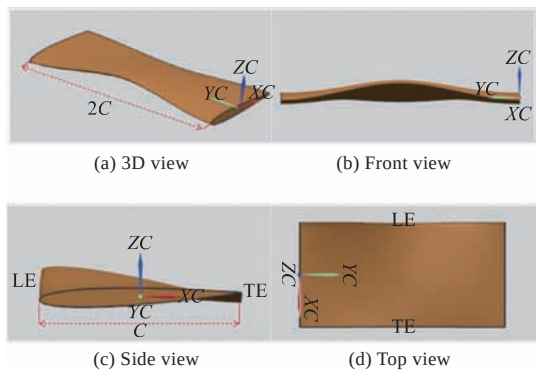

(a) 3D view (b) Front view

(c) Side view (d) Top view

Fig. 1 Geometrical views of Twist11N hydrofoil

length of the section of the side wall boundary and the upper and lower wall boundaries is C, and the spanwise direction is shown by C. The distance between the inlet and the leading edge is $2C$, and that between the outlet and the leading edge is $5C$.

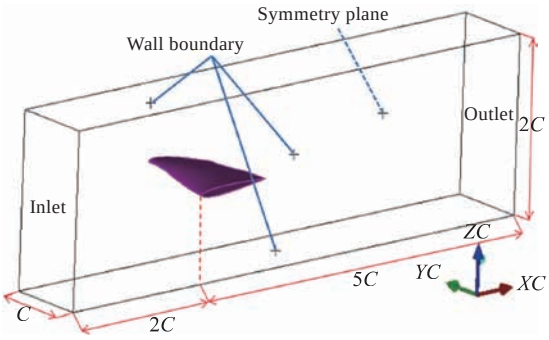

Fig. 2 Calculated domain of half of Twist11 twisted hydrofoil

Hexahedral grids employing the O-H topology are utilized, with the details depicted in Fig. 3. Three sets of grids with different densities are generated by changing the number of nodes on the contour line, including G1 (coarse grid), G2 (medium grid), and G3 (fine grid). The number of nodes in each set of grids is 2.9 million, 3.66 million, and 4.71 million, respectively. In order to reduce the requirement for computing resources, the growth rate of the number of nodes is set to be $\sqrt[4]{2}$. The grid division parameters are shown in Table 1. Specifically, $y^+_{\max}$ denotes the maximum height of the first grid in the wall boundary, $\Delta x+$ represents the average nondimensional grid spacing in the chord length direction and equals $k/[(l_1-1)/2 + (l_3-1)]$, with $k = 112^2$, l_1-l_4 is the number of nodes along the topological line of the hydrofoil.

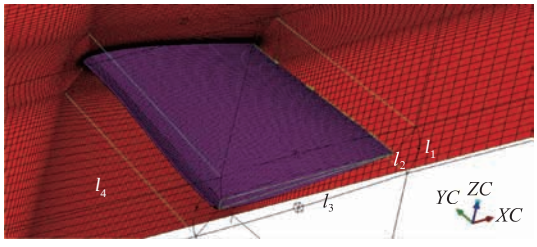

Fig. 3 Division of O-shaped grids around Twist11N hydrofoil

Table 1 Grid parameters of Twist11N hydrofoil

Grid	l_1	l_2	l_3	l_4	$y^+_{\max}$	$\Delta x+$
G1	25	63	101	90	0.793	112
G2	30	75	120	90	0.789	94
G3	36	89	143	90	0.803	80

Numerical analysis is carried out by ANSYS FLUENT 19.0. For the numerical calculation of the unsteady cavity flow around the Twist11N hydrofoil with a cavitation number σ of 1.07, the boundary conditions are set as follows: the inlet velocity V_∞ equals 6.97 m/s; the outlet is defined as pressure outlet, and the pressure p_{out} equals 29.0 kPa according to $\sigma = (p_{out} - p_v)/0.5\rho_1 V_\infty^2$. A slip plane is applied to the upper, lower, and side wall boundaries of the calculated domain, and a non-slip plane is applied to the hydrofoil surface. Furthermore, a symmetry plane is utilized in the midsection of the span. The density, dynamic viscosity coefficient, and vapor pressure of the liquid and vapor phases are set when temperature T equals 24 °C. The time step is determined according to ($\Delta t = T_{ref} / 200$, $T_{ref} = C/V_\infty$) in Ref. [17]. The calculated time step Δt equals 1.076×10^{-4} s, and 1.0×10^{-4} s is chosen as the final time step. 100 iterations per time step are used to balance calculation accuracy and efficiency.

3 Results and discussion

The lift and the drag coefficients are defined as $C_L=F_L/(0.5\rho_1 V_\infty^2 A)$ and $C_D=F_D/(0.5\rho_1 V_\infty^2 A)$, respectively. In addition, the pressure coefficient characterizing the pressure distribution on the upper and lower surfaces of the hydrofoil C_p equals $(p-p_{out})/(0.5\rho_1 V_\infty^2)$, where F_L and F_D represent the lift and drag, respectively, and A is the projected area. In view of the random oscillation characteristic of lift, drag, and pressure coefficients calculated by the LES method, the time averaged lift coefficient $\bar{C}_L$, time averaged drag coefficient $\bar{C}_D$, and time averaged pressure coefficient $\bar{C}_p$ in multiple periods are defined for comparative analysis. The error between experimental and numerical results is denoted as (Calculated value-experimental value)/experimental value × 100%.

Before the simulation, the convergence ratio R_k recommended by the 22nd ITTC is adopted to examine the grid convergence simulated by the wet flow field around the Twist11N hydrofoil based on the LES method. According to calculated results, the time averaged drag coefficients of the three sets of grids with different densities converge monotonically, while the time averaged lift coefficients converge with oscillations, which meets the demands for grid convergence.

3.1 Influence of grid density on numerical simulation of cavitation

On the basis of the WALE model and the LES method, when σ equals 1.07, the cavitation around the Twist11N hydrofoil is simulated by using G1,

G2, and G3, so as to examine the influence of different grid densities on the cavitation shedding frequency, cloud cavity shapes, and the pulsation characteristics of lift and drag coefficients.

As illustrated in Fig. 4, the variation curve of the cavity volume is estimated by using the three sets of grids, and the cavitation shedding frequency f is derived through the Fourier transform. The results show that the cavitation shedding frequency calculated by the three sets of grids are 30.14, 31.78, and 31.24 Hz, respectively, with an error of −7.40%, −2.37%, and −4.02% from the experimental results [4] (f =32.55 Hz). It can be seen that in terms of the cavitation shedding frequency of coarse grids in G1, there is a large error between the calculated value and the experimental value, and errors of the cavitation shedding frequency in G2 and G3 are considerably smaller. In addition, under the current calculation settings, grid refinement does not minimize the error of the cavitation shedding frequency but makes the frequency deviate more from the experimental value.

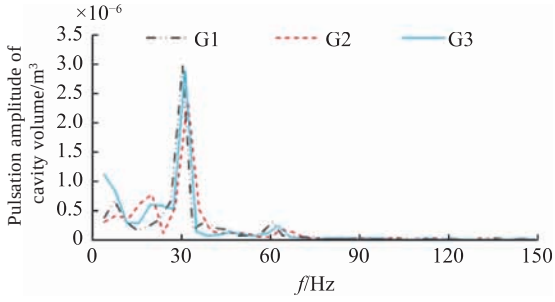

Fig. 4 Cavitation shedding frequency under different grid densities

Fig. 5 shows the predicted cavitation evolution under different grid densities in one period. The cloud cavity shapes at typical Moments 1−9 with α equaling 0.1 are adopted and compared with the experimental results [4]. As shown in the top view, the inflow direction is from top to bottom.

Compared with the experimental results, it can be seen that the three sets of grids can basically simulate the typical characteristics of the evolution process of the unsteady cloud cavitation, and the steps are as follows:

1) Primary shedding. When attached sheet cavities develop to a certain degree, they will break and produce a large-scale cavity cloud.

2) Formation of horseshoe-shaped cavities. The broken attached sheet cavities are concave-shaped and will continue to develop, while the produced cavity cloud rolls up and forms a horseshoe-shaped

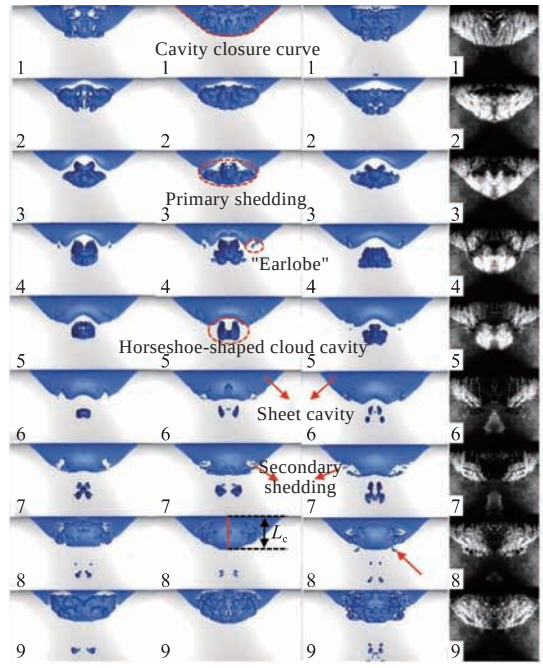

(a) G1 (b) G2 (c) G3 (d) Exp. results[4]

Fig. 5 Comparison of cavitation evolution simulated by different grids and experimental results

structure.

3) Secondary shedding. The horseshoe-shaped cavity cloud goes downstream under the action of the main flow, and the attached sheet cavities shed their small-scale structures at the earlobe position.

4) Cavity collapse. The small-scale cavity cloud that has undergone the secondary shedding will collapse, and the concave-to-convex transition of the attached sheet cavities occurs. In addition, the large-scale horseshoe-shaped cloud cavities collapse in the downstream high-pressure area, while the developed attached sheet cavities break again, and a new period begins.

It can be observed from Fig. 5 that the surface of the sheet cavities that will undergo the primary shedding is relatively rough at Moments 1 and 9 due to re-entrant jets, while that of the sheet cavities at other moments is smoother. The three sets of grids all roughly simulate the phenomenon above. In addition, as the grids get refined, structures of the sheet cavities' upper surfaces get more refined and are similar to that of relevant regions observed by experiments. However, there are still some discrepancies in cavity shapes between numerical and experimental results. For instance, experiments have revealed that sheet cavities have a striped or vesicular shape that does not appear in numerical simulations. This is mostly because the calculated shape is defined by continuous fractions.

Due to different grid densities, there are some dis-

crepancies in cavity shapes captured during the numerical simulation of cavitation evolution, and they are described as follows:

1) Cavity length L_c (Moment 8 in Fig. 5(b)). According to the variation of L_c/C values calculated under different grid densities over one period in Fig. 6, it can be observed that the growth rate of L_c tends to slow down over time, which can be explained by the fact that as the sheet cavities reach a certain length, the sheet cavities in the middle of the low span are lifted and rolled over under the influence of re-entrant jets and the main inflows, which prevents the sheet cavities from developing downstream. Moreover, the L_c/C values predicted by G1 are much lower than those predicted by G2 and G3 at corresponding moments, and the values predicted by G2 and G3 are more in line with experimental results [4]. Specifically, the L_c/C values predicted by G3 deviate more from the experimental results at most moments than those predicted by G2, which can be seen from cavity shapes in Fig. 5.

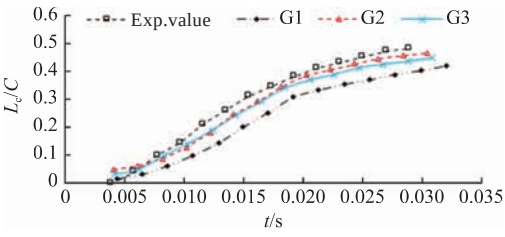

Fig. 6 Comparison of L_c/C values calculated under different grid densities

2) Secondary shedding. As can be seen from the cavity evolution, G1 results in simple cavitation at the earlobe position, while G2 and G3 result in a pronounced secondary shedding in the same position. According to the arrowed positions at Moments 1 and 8 in Fig. 5(c), more refined cavitation is captured after grid refinement.

3) Scale of horseshoe-shaped cloud cavities. As shown in Fig. 5, the horseshoe-shaped cloud cavities generated by the primary shedding can be observed in the three sets of grids. Besides, the cloud cavities after shedding all have a V-shaped structure in the upper section at Moment 3, and their shapes are similar. At Moment 4, the initial state of the horseshoe-shaped cloud cavities is visible, with the cloud cavity inclination in numerical results of G3 different from that of G1 and G2.

In general, the cloud cavitation simulated by the three sets of grids is consistent during Moments 1-4. After Moment 4, the evolution of cloud cavitation is accompanied by shrinkage and collapse, and the small-scale cavities formed by the collapse are closer to the grid scale magnitude. In addition, different grid scales result in changes in the precision of predicting turbulent flow characteristics, including the vortex scale that can be captured in the flow field. It can be seen that after Moment 4, the shape differences in the horseshoe-shaped cloud cavities are apparent. Besides, the spanwise scale at the stable state simulated by G1 is smaller than the experimental results, while the simulated results of G2 and G3 are both similar to the experimental results.

The variation curves of the lift and drag coefficients over one period simulated by the three sets of grids are depicted in Figs. 7 and 8, respectively. In the figures, the non-dimensional time t/T is the horizontal coordinate axis, and T is the period of the corresponding grid density. According to the figures, the lift and drag pulsation characteristics calculated by G1 are relatively small, and the transient pulsations of the lift and drag coefficients in the three sets of grids are relatively consistent and centered in the intervals of t/T=[0.2, 0.3] and [0.8, 1.0]. The difference in calculated lift and drag pulsations between the three sets of grids mainly appears in the second half of the period and is closely related to the collapse of the horseshoe-shaped cloud cavities. In addition, by comparing the evolution process of the horseshoe-shaped cloud cavities simulated by the three sets of grids, it can be found that the collapse and rebound of the horseshoe-shaped cloud cavities simulated by G2 and G3 are more obvious than those by G1 (e. g., Moments 5−8 in Fig. 5), which also explains the violent lift and drag pulsations predicted by G2 and G3.

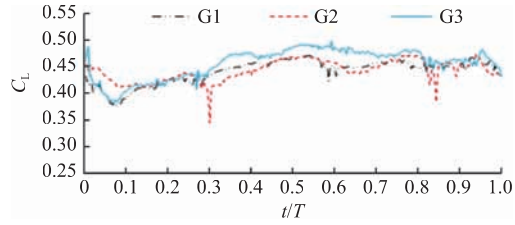

Fig. 7 Variation curves of lift coefficients under different grid densities in one period

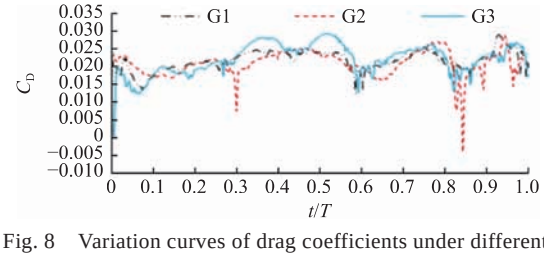

Fig. 8 Variation curves of drag coefficients under different grid densities in one period

Table 2 shows the time averaged lift and drag coefficients of multiple periods calculated by the three sets of grids, which are compared with the experimental lift coefficient [18] ($\bar{C}_L$=0.51) and the calculated results based on the LES method in Ref. [19]. According to the table, as the grids get refined, the time averaged lift coefficient is closer to the experimental values. The error between the predicted and experimental value of $\bar{C}_L$ in G3 is 11.71%, with a deviation of 2.34% from the results in Ref. [19]. In addition, there is a large error between the calculated and experimental value of the time averaged lift coefficient, which may be explained by the fact that the sensor is damaged under the cavitation collapse, which results in a failure of some experimental results [19].

Table 2 Comparison of time averaged lift and drag coefficients under different grid densities

Item	G1	G2	G3	LES[19]
$100\bar{C}_D$	2.117	2.084	2.116	–
$\bar{C}_L$	0.4412	0.4458	0.4503	0.4400
$\bar{C}_L$ error/%	−13.49	−12.59	−11.71	−13.73

Figs. 9 and 10 display the time averaged pressure coefficient $-\bar{C}_p$ around the hydrofoil at YC = 0.12 m and YC = 0.15 m in the spanwise direction, as well as the comparison of the results by two experiments (i.e., the experiments conducted by Delft and EPFL that are two different cavitation water tanks) under different grid densities in the cavity flow. Notably, the size of the Delft hydrofoil is twice that of the EPFL hydrofoil, and they both are examined at the same Reynolds number. Due to the unreliability of the experimental data at some pressure monitoring stations [20], $\bar{C}_p$ in the experimental results of the Delft [18] and the EPFL [18] with the same size are compared. According to the figures, at the two sections of hydrofoil in the spanwise direction, the calculated time averaged pressure coefficients on the pressure surface with different grid densities are essentially the same, but those on the suction surface are slightly different. This is reflected primarily in the following aspects.

1) In the region of $0 < x/C < 0.4$, the pressure is low, and there are attached sheet cavities. The probability of violent cavity collapse is low, and the distribution and change trend of $-\bar{C}_p$ in the two sections are relatively consistent.

2) In the region of $0.4 \leqslant x/C \leqslant 0.5$, which is the end of the sheet cavities, the pressure distribution in

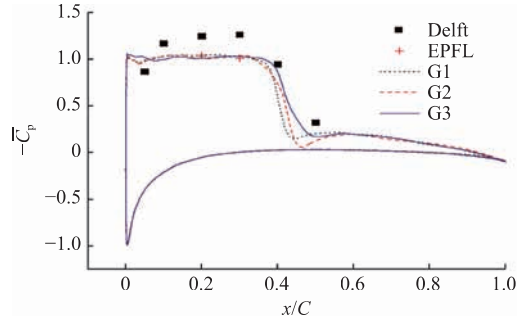

Fig. 9 $\bar{C}_p$ distribution around hydrofoil surface at YC = 0.12 m in the spanwise direction

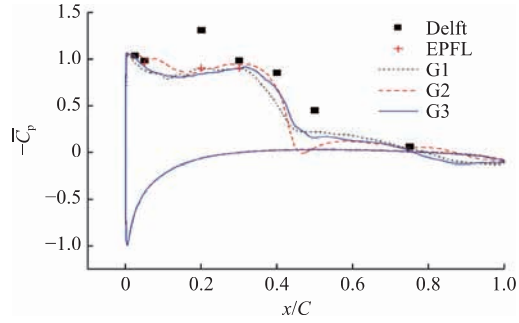

Fig. 10 $\bar{C}_p$ distribution around hydrofoil surface at YC = 0.15 m in the spanwise direction

the chord length direction varies significantly, and for the spanwise position with YC=0.12 m, the pressure transition trend predicted by G3 is closer to the experimental result, while for the spanwise position with YC=0.15 m, G2 better simulates the pressure transition trend at x/C=0.4.

3) In the region of $0.5 < x/C < 1$, the pressure distribution at various positions along the span is altered in the same manner. This is because there is a specific distance between the position of YC=0.12 m and the horseshoe-shaped cloud cavity shedding at the center of the span, and the influence of its development and collapse are quite small. The distribution of $-\bar{C}_p$ is essentially the same. The area at YC= 0.15 m in the spanwise direction is where horseshoe-shaped cloud cavities develop and collapse, and the predicted distribution of $-\bar{C}_p$ is a little different because the horseshoe-shaped cloud cavities and vortex structures predicted by different grid densities are different.

3.2 Influence of SGS models on numerical simulations of cavitation

Based on the G2-oriented LES method, this paper adopts WALE, WMLES, and SL models to carry out numerical simulations of cavitation around the Twist11N hydrofoil at σ = 1.07 and analyzes the influence of SGS models on the cavitation shedding frequency, cloud cavity shapes, and the

pulsation characteristics of lift and drag coefficients of the hydrofoil.

Fig. 11 shows the cavitation shedding frequency f calculated by the three SGS models. The results show that the shedding frequency calculated by the WALE, WMLES, and SL models are 31.78, 29.19, and 34.87 Hz, respectively, with an error of −2.37%, −10.32%, and 7.13% from the experimental results [4] (f = 32.55 Hz). The error of the shedding frequency calculated by the WALE model is the smallest.

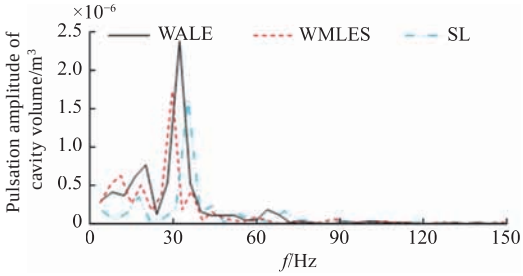

Fig. 11 Cavitation shedding frequency calculated by different SGS models

Fig. 12 shows the cavitation evolution process predicted by different SGS models within a certain period. Similarly, the isosurface with α = 0.1 is used to show the shape of cloud cavities at typical moments, and the results are compared with the experimental results.

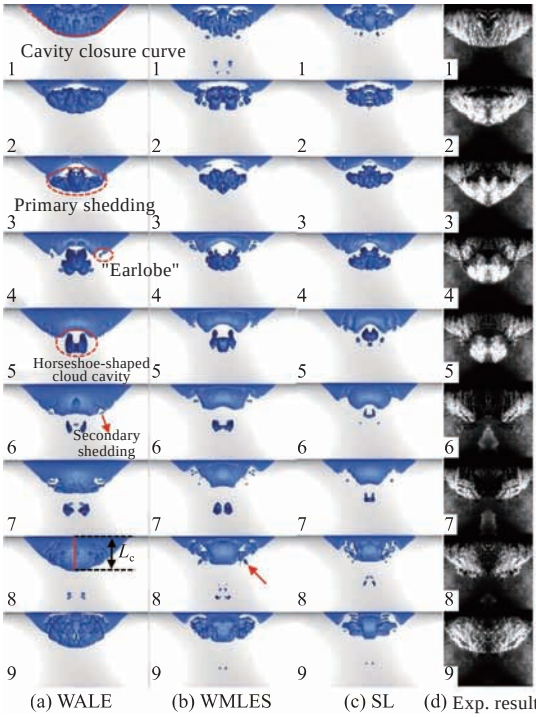

Fig. 12 Comparison of cavitation evolution simulated by different SGS models and experimental results

As Fig. 12 shows, compared with the experimental results, the three models can basically simulate the typical characteristics of the evolution of unsteady cloud cavitation, but the simulated cavity shapes vary greatly, which can be shown in the following aspects.

1) The closed curve contour of sheet cavities. By comparing the chord length direction range of sheet cavities (Moment 9 in Fig. 12), the paper found that the results calculated by the WALE model are in good agreement with the experimental results. When the maximum size of the sheet cavities is reached, the chord length direction can be increased by approximately 50%. In addition, the results calculated by the WMLES and SL models are relatively small, and the chord length direction only increases by around 40%. However, the length in the spanwise direction of sheet cavities is consistent near the leading edges of the three models. Furthermore, as depicted in Fig. 13, the L_c/C values calculated by several SGS models in one period vary with time. It can be seen that the L_c/C values calculated by the WMLES and SL models are consistent but much lower than the experimental results [4]. However, the L_c/C value calculated by the WALE model is in good agreement with the experimental results.

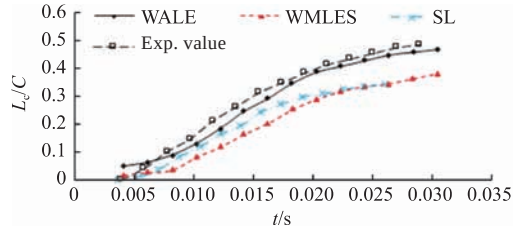

Fig. 13 Comparison of L_c/C values calculated by different SGS models

2) Secondary shedding. The experimental results from Moments 3−7 in Fig. 12 show that the area that is unstable due to re-entrant jets in the earlobe position of the sheet cavities expands gradually. However, the cavitation structures in the area calculated by the WMLES and SL models are much sparser compared with the experimental results, especially by the SL model. However, rich small-scale cavitation structures in this area are observed based on the WALE model.

3) Horseshoe-shaped cloud cavities. From a top-down perspective, the scale range of the horseshoe-shaped cloud cavities obtained by the WALE and WMLES models is in good agreement with the experimental results, while that calculated by the SL model is significantly smaller than the experimental results. For the development of horseshoe-shaped cloud cavities in the middle of the span, the WM-

LES model can simulate the phenomenon that the horseshoe-shaped cloud cavities formed by primary shedding in the preceding period are about to pass the trailing edges on the hydrofoil surface at Moment 1, while the horseshoe-shaped cloud cavities observed by the other two models collapse in advance.

Table 3 shows the time averaged lift coefficient $\bar{C}_L$ and drag coefficient $\bar{C}_D$ of multiple periods calculated by the three SGS models, which are compared with the experimental lift coefficient [18] ($\bar{C}_L$= 0.51) and the calculated results based on the LES method in Ref. [19]. For $\bar{C}_L$ its value predicted by the three models is too low, with the WALE model yielding the lowest error from the experimental results, the WMLES model yielding the second lowest error, and the SL model yielding the highest error. However, the results based on the WALE model are closer to those presented in Ref. [19].

Table 3 Comparison of time averaged lift and drag coefficients in different SGS models

Item	WALE	WMLES	SL	LES[19]
$100\bar{C}_D$	2.084	2.582	2.564	–
$\bar{C}_L$	0.4458	0.4156	0.3660	0.4400
$\bar{C}_L$ error/%	−12.59	−18.51	−28.24	−13.73

Figs. 14 and 15 compare the time averaged pressure coefficient $\bar{C}_p$ calculated by different SGS models with the experimental values [18] at YC = 0.12 m and YC = 0.15 m in the spanwise direction, respectively. At YC = 0.12 m and YC = 0.15 m, the distribution difference of $-\bar{C}_p$ in the suction surface calculated by different SGS models is reflected mostly in the interval of $0.3 \leqslant x/C \leqslant 0.5$. According to the figures, the low-pressure region calculated by the WALE model is longer than that by the WMLES and SL models, which indicates that the extension length of sheet cavities predicted by the WALE model is longer, and this is consistent with the phenomenon observed in the cavitation evolution process. At the same time, the pressure coefficient predicted by the WALE model varies in the interval of $0.3 \leqslant x/C \leqslant 0.4$ and is in good agreement with the experimental results.

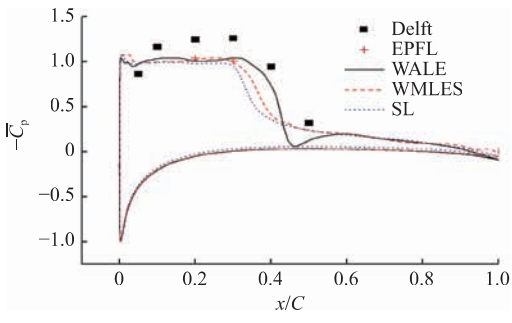

Fig. 14 $\bar{C}_p$ distribution around hydrofoil surface at YC = 0.12 m in the spanwise direction

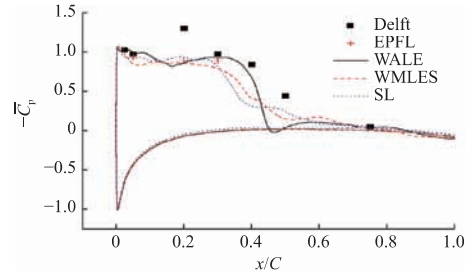

Fig. 15 $\bar{C}_p$ distribution around hydrofoil surface at YC = 0.15 m in the spanwise direction

4 Conclusions

Based on the LES method and the S-S cavitation model, this paper investigates the cavitation evolution, cavitation shedding frequency, and the lift and drag coefficients around a Delft Twist11N 3D twisted hydrofoil by using three sets of grids with different densities and three SGS models. The following conclusions can be obtained.

1) On the premise of the maximum surface boundary $y^+ < 1$, when the average non-dimensional grid spacing in the streamwise direction meets the condition of $\Delta x+ \leqslant 94$, the numerical simulation with the specific grid density can not only capture the unsteady cavitation evolution such as the shedding of small-scale cavitation and the inception and collapse of the horseshoe-shaped cloud cavities but also obtain accurate cavitation shedding frequency, time averaged lift and drag coefficients, and time-averaged pressure distribution.

2) All three SGS models can reproduce the typical characteristics of the evolution process of unsteady cloud cavitation. Compared with that by the WMLES and SL models, the evolution of sheet and cloud cavities captured by the WALE model are in good agreement with experimental results, and the predicted cavitation shedding frequency, time averaged lift and drag coefficients, and pressure coefficient are more accurate.

Therefore, the LES method based on the WALE model is recommended for numerical simulation of unsteady cloud cavitation.

References

[1] KUBOTA A, KATO H, YAMAGUCHI H, et al. Unsteady structure measurement of cloud cavitation on a foil section using conditional sampling technique [J]. Journal of Fluids Engineering, 1989, 111 (2): 204−210.

[2] KJELDSEN M, ARNDT R E A, EFFERTZ M. Spec-

tral characteristics of sheet/cloud cavitation [J]. Journal of Fluids Engineering, 2000, 122 (3): 481−487.

[3] FARHAT M, AVELLAN F. On the detachment of a leading edge cavitation [J]. Cerâ mica, 2001, 49 (309): 40−43.

[4] FOETH E J. The structure of three-dimensional sheet cavitation [D]. The Netherlands: Delft University of Technology, 2008.

[5] LI D Q, GREKULA M, LINDELL P. A modified SST *k*-*ω* turbulence model to predict the steady and unsteady sheet cavitation on 2D and 3D hydrofoils [C]// The 7th International Symposium on Cavitation. Ann Arbor, MI, USA: CAV Publishing, 2009: 1−13.

[6] LIU D C; HONG F W. The numerical analysis of unsteady performance of cavitating flow on 3D hydrofoils and comparison with experiments [J]. Chinese Journal of Hydrodynamics, 2010, 25 (6): 721−726 (in Chinese).

[7] LI Z R. Assessment of cavitation erosion with a multiphase Reynolds-averaged Navier-Stokes method [D]. The Netherlands: Delft University of Technology, 2012.

[8] JI B, LUO X W, ARNDT R E A, et al. Numerical simulation of three dimensional cavitation shedding dynamics with special emphasis on cavitation-vortex interaction [J]. Ocean Engineering, 2014, 87: 64−77.

[9] PU J J, XIONG Y. Numerical study of hydrofoil tip vortex fluid field [J]. Chinese Journal of Ship Research, 2017, 12 (1): 8−13, 26 (in Chinese).

[10] JI B, LUO X W, ARNDT R E A, et al. Large eddy simulation and theoretical investigations of the transient cavitating vortical flow structure around a NACA66 hydrofoil [J]. International Journal of Multiphase Flow, 2015, 68: 121−134.

[11] WU X C, WANG Y W, HUANG C G. Effect of mesh resolution on large eddy simulation of cloud cavitating flow around a three dimensional twisted hydrofoil [J]. European Journal of Mechanics-B/Fluids, 2016, 55: 229−240.

[12] LONG X P, CHENG H Y, JI B, et al. Large eddy simulation and Euler-Lagrangian coupling investigation of the transient cavitating turbulent flow around a twisted hydrofoil [J]. International Journal of Multiphase Flow, 2018, 100: 41−56.

[13] SUN T Z, WANG Z H, ZOU L, et al. Numerical investigation of positive effects of ventilated cavitation around a NACA66 hydrofoil [J]. Ocean Engineering, 2020, 197: 106831.

[14] LILLY D K. A proposed modification of the Germano subgrid-scale closure method [J]. Physics of Fluids A: Fluid Dynamics, 1992, 4 (3): 633−635.

[15] NICOUD F, DUCROS F. Subgrid-scale stress modelling based on the square of the velocity gradient tensor [J]. Flow, Turbulence and Combustion, 1999, 62 (3): 183−200.

[16] SHUR M L, SPALART P R, STRELETS M K, et al. A hybrid RANS-LES approach with delayed-DES and wall-modelled LES capabilities [J]. International Journal of Heat and Fluid Flow, 2008, 29 (6): 1638−1649.

[17] COUTIER-DELGOSHA O, REBOUD J L, DELANNOY Y. Numerical simulation of the unsteady behaviour of cavitating flows [J]. International Journal for Numerical Methods in Fluids, 2003, 42 (5): 527−548.

[18] HOEKSTRA M, VAN TERWISGA T, FOETH E J. SMP'11 workshop-case 1: delftfoil [C]//2nd International Symposium on Marine Propulsors. Hamburg, Germany: ISMP Publishing, 2011: 1−6.

[19] BENSOW R E. Simulation of the unsteady cavitation on the Delft Twist11 foil using RANS, DES and LES [C]//2nd International Symposium on Marine Propulsors. Hamburg, Germany: ISMP Publishing, 2011: 1−10.

[20] VAZ G, LLOYD T P, GNANASUNDARAM A K. Improved modelling of sheet cavitation dynamics on Delft Twist11 hydrofoil [C]//VII International Conference on Computational Methods in Marine Engineering. Nantes, France: ICCMME Publishing, 2017.

亚格子模型对三维扭曲水翼空化现象的影响

何朋朋[1,2], 李子如[1,2], 张孝旺[1,2], 贺伟*[1,2]

1 武汉理工大学 高性能舰船技术教育部重点实验室, 湖北 武汉 430063

2 武汉理工大学 船海与能源动力工程学院, 湖北 武汉 430063

摘　要: [**目的**] 旨在探究三维扭曲水翼空化数值模拟中网格密度及亚格子模型的适应性问题。[**方法**] 为此, 使用大涡模拟(LES)方法和Schnerr-Sauer(S-S)空化模型对Delft Twist11N三维扭曲水翼的非定常空化流场进行数值模拟, 重点研究3套不同密度的网格和WMLES, SL, WALE这3种亚格子模型对Delft Twist11N水翼空化演变过程、空化脱落频率及时均升阻力系数等的影响。[**结果**] 结果表明: 适当的网格加密形式既能够捕捉到较多的细小空泡脱落、马蹄形云空泡的初生与溃灭等非定常空化演变现象, 又能够获得具有较高精度的空泡脱落频率、时均升阻力系数和时均压力分布。相较于WMLES和SL亚格子模型, WALE亚格子模型较好地捕捉到了片空泡及云空泡的演变, 在预报空泡脱落频率、时均升阻力系数及压力系数方面精度较优。[**结论**] 因此, 推荐采用基于WALE亚格子模型的LES方法进行非定常云状空化的数值模拟。

关键词: 三维扭曲水翼; 云状空泡; 大涡模拟; 亚格子模型; 网格密度